Unveiling the charge storage mechanism in non-aqueous and

aqueous Zn/Na₃V₂(PO₄)₂F₃ batteries

Min Je Park and Arumugam Manthiram*

Materials Science and Engineering Program & Texas Materials Institute

The University of Texas at Austin, Austin, TX 78712, USA

Corresponding Author

*E-mail: manth@austin.utexas.edu, Phone: (512) 471-1791

ABSTRACT

In search of a suitable cathode host for aqueous Zn-ion batteries (ZIBs), polyanionic

materials have been explored due to their open-framework structure that is believed to improve

Zn-ion diffusion. Among them, Na₃V₂(PO₄)₂F₃ was recently shown in the aqueous ZIB to exhibit

attractive electrochemical performance, and the charge storage mechanism was attributed to

reversible Zn²⁺ insertion into the cathode. Here, however, we investigate the puzzling differences

in the electrochemical behavior of Na₃V₂(PO₄)₂F₃ as a cathode material between non-aqueous and

aqueous ZIBs. Ex-situ analyses of the cathode after cycling in both systems unveil that the

observed disparity in the electrochemical behavior stems from the difference in the charge storage

mechanism. In the non-aqueous ZIB, guest ions are determined to be both Zn²⁺ and

Na⁺ initially that gradually shifts to be pure Zn²⁺. In the aqueous ZIB, however, H⁺ is found to be

the guest ion species rather than Zn²⁺. This explains the attractive electrochemical performance in

1

the aqueous ZIB as H⁺ insertion and diffusion would be extremely facile unlike Zn²⁺. Moreover, even with Zn(CF₃SO₃)₂ electrolyte, the formation of zinc salt byproduct on the cathode after discharge further supports that H⁺ ions are inserted into the cathode, as observed with aqueous ZnSO₄ electrolyte. This byproduct formation on the cathode in the aqueous ZIB system calls for careful analyses to be performed to categorically elucidate that Zn ions are indeed the guest ions at the cathode when investigating cathodes for "Zn-ion" batteries.

Keywords: Aqueous Zn-ion batteries, non-aqueous Zn-ion batteries, Na₃V₂(PO₄)₂F₃, zinc insertion, proton insertion

1. INTRODUCTION

The ever-increasing deployment of electric vehicles, portable electronics, and renewable energy sources has generated a pressing need for efficient electrical energy storage systems. This demand has triggered an explosive surge in the usage of lithium-ion batteries (LIBs). Although LIBs have been considered the most prominent electrical energy storage technology to date due to their higher energy and power density compared to alternatives, further improvements are sought in terms of specific energy and cost. At the same time, there are growing concerns of the availability of lithium and the rise in the cost of lithium due to the predicted growth of the LIB market. In light of this, development of next-generation rechargeable battery chemistries based on the utilization of more earth-abundant metals such as magnesium and zinc are being explored. Among these, aqueous Zn-ion batteries (ZIBs) have gathered much attention owing to their lower cost and improved safety over LIBs. In metal is environmentally benign, and unlike Li metal, it can be used as an anode in aqueous electrolytes because the passivation layer that forms on the surface of Zn metal permits the anode to be kinetically stable.

Over the years, the primary focus of research on aqueous ZIBs has been on finding cathode materials that exhibit attractive electrochemical performance. Inspired by the use of MnO₂ cathode in alkaline batteries, several polymorphs of the MnO₂ family have been explored, including those with tunnel structures such as hollandite- (α) , nsutite- (γ) , and todorokite-types, and others such as the layered birnessite- (δ) and spinel- (λ) types.^{7–13} Another area of interest has been vanadium-based oxides and bronzes and their hydrated phases. It has been shown that monovalent or divalent cations in the vanadium oxide bronzes can act as pillars to stabilize the parent structure from irreversible phase transformations during cycling. Also, the presence of water molecules in the vanadium oxides increases the layer spacing, allowing for reversible insertion of hydrated Zn²⁺,

thus improving solid-state Zn-ion diffusion.^{14–17} Prussian blue analogues have also been investigated as their open-framework structure may improve Zn-ion diffusion.^{18,19}

On a similar note, polyanionic host materials with a three-dimensional open-framework structure have been studied more recently. Reversible cycling of NASICON-structured $Na_3V_2(PO_4)_3$ wrapped in graphene-like carbon in aqueous ZIBs was presented.²⁰ The cathode exhibited a discharge plateau at 1.05 V with an initial discharge capacity of 97 mA h g⁻¹, 74 % of which was retained after 100 cycles at a rate of 0.5C. In addition, 60 % (58 mA h g⁻¹) of the initial capacity was attainable even during discharge at 10C rate, demonstrating excellent rate capability. Another work investigated carbon-coated $Na_3V_2(PO_4)_2F_3$ as the cathode which also presented outstanding cycling and rate capability.²¹ By modifying the Zn-metal anode, 95 % of the initial discharge capacity (48 mA h g⁻¹) was retained after 4,000 cycles at a remarkable specific current density of 1 A g⁻¹ (16C). Due to the inductive effect of fluorine in vanadium fluorophosphates, an even higher discharge voltage (1.62 V) was obtained compared to that of NASICON-structured $Na_3V_2(PO_4)_3$ (1.05 V). Both reports claimed that their exceptional electrochemical performance was achievable due to facile Zn^{2+} insertion and diffusion into the cathode hosts.

In our previous investigation of the NASICON-related $V_2(PO_4)_3$ —also with a three-dimensional polyanionic open-framework structure—as a host for Zn^{2+} insertion in a non-aqueous Zn-ion electrolyte, however, it was discovered that Zn^{2+} diffusion was severely hindered within the host, and required an elevated temperature of 80 °C for appreciable insertion to occur.²² The arduous nature of multivalent-ion (Mg^{2+} and Zn^{2+}) diffusion has also been emphasized in recent studies exploring close-packed structures like the spinel phase.^{23–26} In addition, due to the strong interaction between the Zn ions and the host framework, the structural integrity of the host was not maintained, leading to poor cycle life. This apparent discrepancy of Zn-ion insertion and de-

insertion in a polyanionic cathode host between the non-aqueous and aqueous ZIB systems seems puzzling and suggests that fundamental differences may be present.

Furthermore, in contrast to LIBs, for which the mechanism of energy storage is established as the reversible intercalation of Li-ions in the cathode during cycling, different energy storage mechanisms have been proposed for aqueous ZIBs.²⁷ While many studies on cathode materials in aqueous ZIBs report reversible Zn²⁺ insertion into the cathode host as the reaction mechanism for electrochemical energy storage, 8,14,20,21,28 an increasing number of reports on oxide hosts claim that the reaction at the cathode involves either co-insertion of both Zn²⁺ and H⁺, ^{13,16,29} or a conversion reaction involving H⁺ insertion.^{7,30} Recently, H⁺ insertion has been shown to be the dominant charge storage mechanism for layered and tunneled oxide hosts in aqueous ZIBs. 31-33 This charge storage mechanism may also hold true for three-dimensional open-framework structures like polyanionic cathode hosts that have shown excellent electrochemical performances in aqueous ZIBs. Elucidating the reaction mechanism of each cathode material is imperative for developing suitable cathode materials for multivalent-ion insertion. If reversible Zn-ion insertion into a given cathode material is achievable then it can be applied to not only ZIBs, but also to other multivalention batteries utilizing metal anodes of more negative reduction potential (e.g., Mg²⁺ and Al³⁺), leading to development of higher energy density multivalent-ion batteries.

Hence, to determine the underlying cause of the noticeable difference in the electrochemical behavior of the open-framework polyanionic hosts between the non-aqueous and aqueous ZIB systems, $Na_3V_2(PO_4)_2F_3$ which was reported as a cathode for facile Zn-ion insertion, is investigated, and its electrochemical energy storage mechanisms in non-aqueous (no H⁺ can be present) and aqueous (both Zn^{2+} and H⁺ can be present) ZIB systems are presented. Electrochemical cycling of $Na_3V_2(PO_4)_2F_3$ cathode performed in both non-aqueous and aqueous

ZIBs show that its electrochemical behavior is completely different in each system. *Ex-situ* X-ray diffraction (XRD) and elemental analyses on the $Na_3V_2(PO_4)_2F_3$ cathode after cycling in the non-aqueous cell reveal that Zn^{2+} acts as the guest ion. However, the same analyses as well as Fourier transform-infrared (FT-IR) analyses performed on the cathode after cycling in the aqueous electrolyte show that H^+ is the guest ion rather than Zn^{2+} . This difference in the energy storage mechanism results in a marked difference in the electrochemical performance of the $Na_3V_2(PO_4)_2F_3$ cathode.

2. EXPERIMENTAL SECTION

2.1. Synthesis of Na₃V₂(PO₄)₂F₃/C (NVPF/C). The synthesis was performed in two steps. First, VPO₄/C was synthesized through a sol-gel method. In a beaker filled with deionized water (DIW), 10 mmols of V₂O₅ (1.82 g, Sigma Aldrich, 99.6+%) and 30 mmols of C₂H₂O₄.2H₂O (3.78 g, Fisher Scientific, 99.5%) were added. The mixture was heated and stirred at 80 °C to dissolve all of the V₂O₅, forming a clear blue solution. Then 10 mmols of NH₄H₂PO₄ (2.30 g, Fisher Scientific, \geq 98.0%) was added to the solution. The solution was heated and stirred until most of the DIW was removed. The remaining DIW was completely removed by placing the beaker in an oven at 100 °C overnight. The dried precursor was then collected, ground with a mortar and pestle, and heated in a tube furnace at 350 °C for 6 h under Ar flow. After heating, the intermediate powder was collected and mixed with Super P (20 wt. %) with a planetary ball mill (Pulverisette 6, Fritsch) at 400 rpm for 6 h to obtain a homogeneous mixture. The mixture was then pressed into a pellet and heated at 800 °C for 10 h under Ar flow to form the crystalline VPO₄/C powder. The obtained VPO₄/C was then mixed with NaF (Alfa Aesar, 99 %) in a molar ratio of 2 : 3.05 with the planetary ball mill at 400 rpm for 6 h. A slight excess of NaF was added to ensure the synthesis

of stoichiometric NVPF. The mixture was then pressed into a pellet and heated in a tube furnace at 600 °C for 8 h under Ar flow, resulting in the formation of NVPF/C.

2.2. Electrochemical Measurements. The NVPF/C cathode was prepared by drop-casting a slurry onto a 5×8 mm (0.4 cm²) Ti foil current collector and drying in a vacuum oven at 120 °C overnight. The slurry consisted of 70 wt. % active material, 15 wt. % Super P, and 15 wt. % polyvinylidenefluoride (PVdF) dispersed in N-Methyl-2-pyrrolidone (NMP). For electrochemical measurements with a non-aqueous Zn-ion electrolyte, custom-made two-electrode flooded cells were constructed. The slurry-coated cathode was attached to a graphite rod with a conductive paste made of Super P and PVdF (1: 1 by wt.) dispersed in NMP. 5×30 mm (1.5 cm²) Zn foil prepared from a rolled Zn-metal shot (Fisher Scientific, 99.99%) was used as the anode. The graphite rod and Zn-metal foil were electrically connected using Inconel wires. In an Ar-filled glovebox, the two electrodes were immersed in 1 mL of 0.3 M Zn(CF₃SO₃)₂ in acetonitrile (AN) electrolyte in a sealed glass tube. For electrochemical measurements with an aqueous Zn-ion electrolyte, CR2032 type coin cells were assembled in ambient conditions. For the Zn anode, the Zn shots were melted and casted in a graphite mold to make an ingot. Then, a piece of that ingot was rolled and punched to prepare 18 mm diameter Zn discs. The Zn disc, slurry-coated Ti foil, and glass fiber filter (Merck Millipore, APFA04700) were used, respectively, as the anode, cathode, and separator. A 3.0 M Zn(CF₃SO₃)₂ aqueous solution was used as the electrolyte. Cyclic voltammetry (CV) and galvanostatic cycling measurements, respectively, were conducted with a Bio-Logic VMP3 potentiostat and an Arbin BT-2000 battery cycler. All electrochemical measurements were carried out at room temperature.

2.3. Materials Characterization. X-ray diffraction patterns were acquired with a Rigaku Miniflex 600 X-ray diffractometer with a Cu K α (λ = 1.5404 Å) radiation source for structural

characterization. On the powder diffraction pattern of the synthesized NVPF/C, Rietveld refinement was conducted using GSAS-II software.³⁴ A FEI Quanta 650 field-emission scanning electron microscope (SEM) equipped with a Bruker detector for energy dispersive X-ray spectroscopy (EDX) was utilized for both morphological and elemental analysis. Thermogravimetric analysis (TGA) was conducted with a Netsch STA 449 F3 instrument under air flow. FT-IR spectra of samples in KBr pellets were acquired with a Thermo Scientific Nicolet iS5 FT-IR spectrometer under N₂ flow. All samples and KBr powder were dried in a vacuum oven at 80 °C prior to conducing the measurements, and OMNIC software atmospheric correction was applied.

3. RESULTS AND DISCUSSION

3.1 Synthesis of NVPF/C. This involved two steps, similar to previously reported methods $^{35-37}$ in which the synthesis of the VPO4 precursor was followed by a solid-state synthesis of NVPF. Additional carbon (Super P, 20 wt. %) was introduced in the VPO4 synthesis to ensure that vanadium is completely reduced to the +3 oxidation state during both the VPO4 precursor and NVPF synthesis, resulting in the formation of NVPF/C. XRD was performed on the synthesized NVPF/C to verify the phase. The acquired and calculated diffraction patterns are presented in Figure 1a. Refinement performed on the powder diffraction pattern indicates that the product is mostly pure with ~ 3 wt. % of the NASICON Na $_3$ V $_2$ (PO4) $_3$ impurity, which is suggested to form possibly due to the volatilization of VF $_3$. 37 All of the diffraction peaks arising due to NVPF/C show a good fit to the calculated pattern from the recently reported Na $_3$ V $_2$ (PO4) $_2$ F $_3$ structure with a subtle orthorhombic distortion. NVPF has three different sites for sodium ions: Na $_1$, which is fully occupied and Na $_2$ and Na $_3$, which are partially occupied. Those form a triangular distribution above

the terminal fluorine of the $V_2O_8F_3$ bioctahedra, which causes an orthorhombic distortion (Figure 1b,c).³⁶ SEM images of the powder show that particles of a few hundred nm in size are agglomerated into clusters of a few μ m in size (Fig. 1d and e). Super P carbon and all other constituent elements are homogeneously distributed, as observed in the elemental mapping images in Fig. 1d. Based on the TGA of NVPF/C, the amount of carbon in the sample was determined to be ~ 15 wt. % (Figure S1).

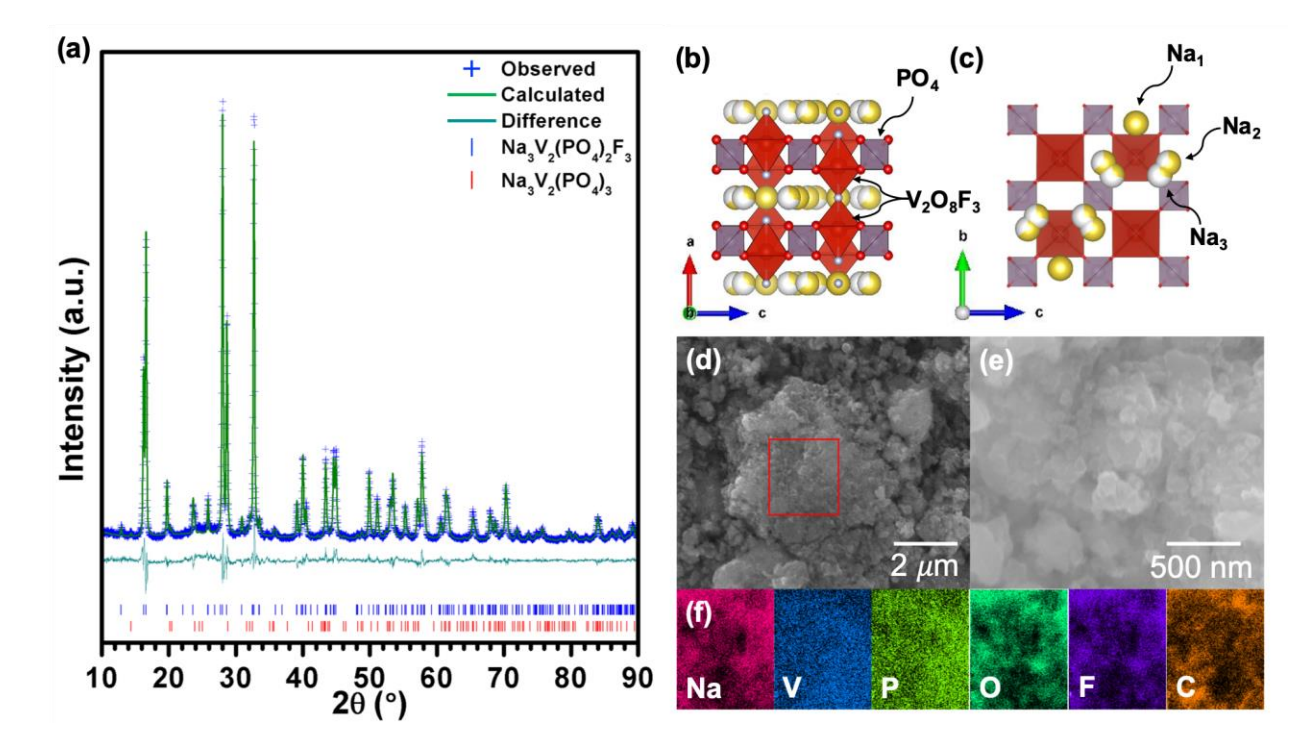


Figure 1. (a) Acquired and refined XRD pattern of NVPF/C, crystal structure of NVPF from (b) a-c plane, (c) b-c plane, (d, e) SEM images of NVPF/C, and (f) EDX mapping of NVPF/C.

3.2. NVPF/C as a Cathode for Aqueous/Non-aqueous Zn-ion Battery. It is understood that if the electrochemical charge and discharge rely on the reversible Zn-ion insertion and deinsertion in the cathode in both the non-aqueous and aqueous Zn-ion cells, a similar but better electrochemical behavior would be observed in the aqueous Zn-ion cell compared to that of the non-aqueous counterpart, with a noticeable difference in the rate capability. This was demonstrated

in a recent report in which the diffusion of Zn^{2+} into the $V_3O_7.H_2O$ cathode from the surface was determined to be more facile in the aqueous electrolyte due to the shielding of the divalent charge of Zn^{2+} by the solvent water molecules, whereas in the non-aqueous electrolyte, a Zn^{2+} ion forms an ion pair with the AN solvent molecule resulting in a higher de-solvation energy at the surface, while exhibiting similar overall electrochemical behavior in both of the systems.¹⁷ Thus, both aqueous and non-aqueous cells were assembled with NVPF/C cathode to compare their electrochemical behaviors.

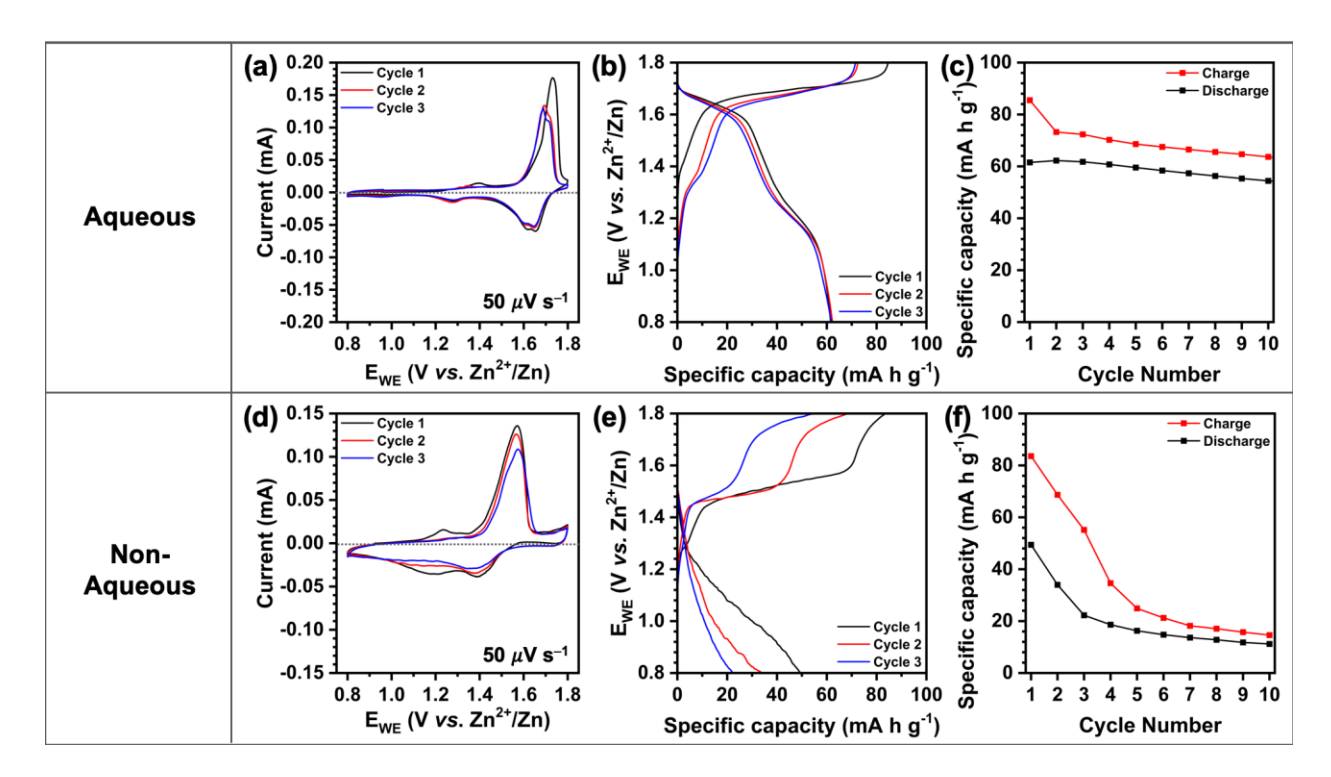


Figure 2. (a) CV, (b) charge and discharge profiles acquired at 1C, and (c) 1C cycling performance of NVPF/C in an aqueous Zn-ion cell. (d) CV, (e) charge and discharge profiles acquired at 0.3C, and (f) 0.3C cycling performance of NVPF/C in a non-aqueous Zn-ion cell.

As presented in the CV plots in Figure 2a,d, NVPF/C is shown to be redox active in both the aqueous and non-aqueous Zn-ion cell with clear anodic and cathodic responses. For both systems, the anodic peak of the first cycle arises as a result of pure Na⁺ removal from the NVPF/C.

By charging up to 1.8 V, one Na per formula unit would be extracted to result in the formation of Na₂V₂(PO₄)₂F₃. In a typical sodium-ion cell, NVPF/C would exhibit three biphasic reactions along with the formation of two intermediate phases before forming the final Na₂V₂(PO₄)₂F₃ phase. However, electrochemically only two plateaus—two biphasic reactions—with a difference of 20 mV would be observed as elucidated in the recent report.³⁸ The scan rate of the CV for both systems may have been too high to observe the scant difference in the potential of the intermediate phases as only one anodic peak was observed. Other than this, the two systems exhibit marked differences in the electrochemical behavior.

In the CV of the aqueous Zn-ion cell (Figure 2a), a small shoulder at 1.29 V and two closely spaced overlapping peaks are observed between 1.61 and 1.63 V from the first cathodic scan. Also, corresponding anodic current response for the small shoulder occurs at 1.40 V while those for the two closely spaced overlapping cathodic peaks occur at 1.69 V and 1.71 V. These features align with the two plateaus as evident on the galvanostatic charge and discharge profiles (Figure 2b), indicating that even with insertion and de-insertion of other guest ions, NVPF/C undergoes biphasic reactions. In the non-aqueous Zn-ion cell, on the other hand, a very dissimilar faradaic behavior is observed, especially during the cathodic scans in the CV (Figure 2d). Unlike the peaklike reduction current response in the CV of the aqueous Zn-ion cell, a broad reduction current response can be observed. This is believed to be due to the sluggish insertion and diffusion of the guest ions into NVPF/C during the cathodic scan, as determined in our previous study with Zn-ion insertion in the polyanionic NASICON-related V₂(PO₄)₃ host.²² Because of the hindered diffusion of guest ions in the cathode and the resultant overpotential, sloping discharge curves without any plateaus are observed in Figure 2e despite NVPF/C undergoing biphasic reactions during charge and discharge.

Another difference is also evident from the cycling of NVPF/C. Galvanostatic charge and discharge profiles of NVPF/C at a rate of 1C in the aqueous Zn-ion cell (Figure 2b) illustrate that the initial discharge capacity is 61 mA h g⁻¹, which is close to the theoretical capacity for one electron transfer (64 mA h g⁻¹) in NVPF/C. This is well maintained as evidenced by the stable electrochemical cycling observed for the first 10 cycles (Figure 2c). As shown in Figure S2, however, some decay in capacity is evident when cycled up to 30 cycles. In the non-aqueous Znion cell, however, NVPF/C cathode exhibits poor reversibility (Figure 2e). The results of galvanostatic cycling, which was performed at an even lower rate of 0.3C, shows that the initial discharge capacity of the cell is only 49 mA h g⁻¹. Also, it decreases dramatically over the first three cycles and gradually stabilizes at 11 mA h g⁻¹ by the end of 10 cycles (Figure 2f). The cycle life of the non-aqueous Zn-ion cell with NVPF/C (10 cycles) is much shorter than that of the aqueous cell (30 cycles). Further optimization of the system like placing a carbon film on the surface of the Zn anode would significantly improve the cycle life of NVPF/C in the aqueous Znion cell, as demonstrated in a recent report.²¹ The carbon film promotes the homogeneous growth of Zn plates parallel to the anode surface, rather than Zn dendrites that grow perpendicular to the anode surface. Hence, the carbon film not only prevents short-circuiting of the cell from Zn dendrites, but it also improves the coulombic efficiency of the cell by reducing the fresh surface of Zn available for side reactions with the electrolyte. Such optimization for long-term cycling was not pursued, however, as the focus of this study is in elucidating the charge storage mechanism.

Considering the fact that the potential of the Na-ion extraction in the first anodic scan only differs by ~ 160 mV between the aqueous and the non-aqueous systems, and the stark discrepancy in the electrochemical behavior of NVPF/C in the aqueous and non-aqueous Zn-ion cells, it seems that the difference in the guest-ion species in NVPF/C cathode is the underlying cause of the

observed difference between the two systems, rather than the difference in the de-solvation energy of the guest ion at the interface between NVPF/C cathode and the electrolyte due to the difference in the solvents.

3.3. Ex-situ analyses on NVPF/C cathode. To elucidate the guest-ion species participating in the electrochemical reaction of NVPF/C cathode in the aqueous and non-aqueous cells, XRD patterns and EDX spectra were acquired for, respectively, structural and elemental analyses of the electrodes after the 1st and 10th cycles in aqueous and non-aqueous Zn-ion cells. Since the cycling of the cells started with charging of the cell, analyses were performed after complete cycling of the cells (*i.e.*, in the discharged state) to observe both the changes in structure after the guest-ion insertion and the nature of those guest ions in the cathode.

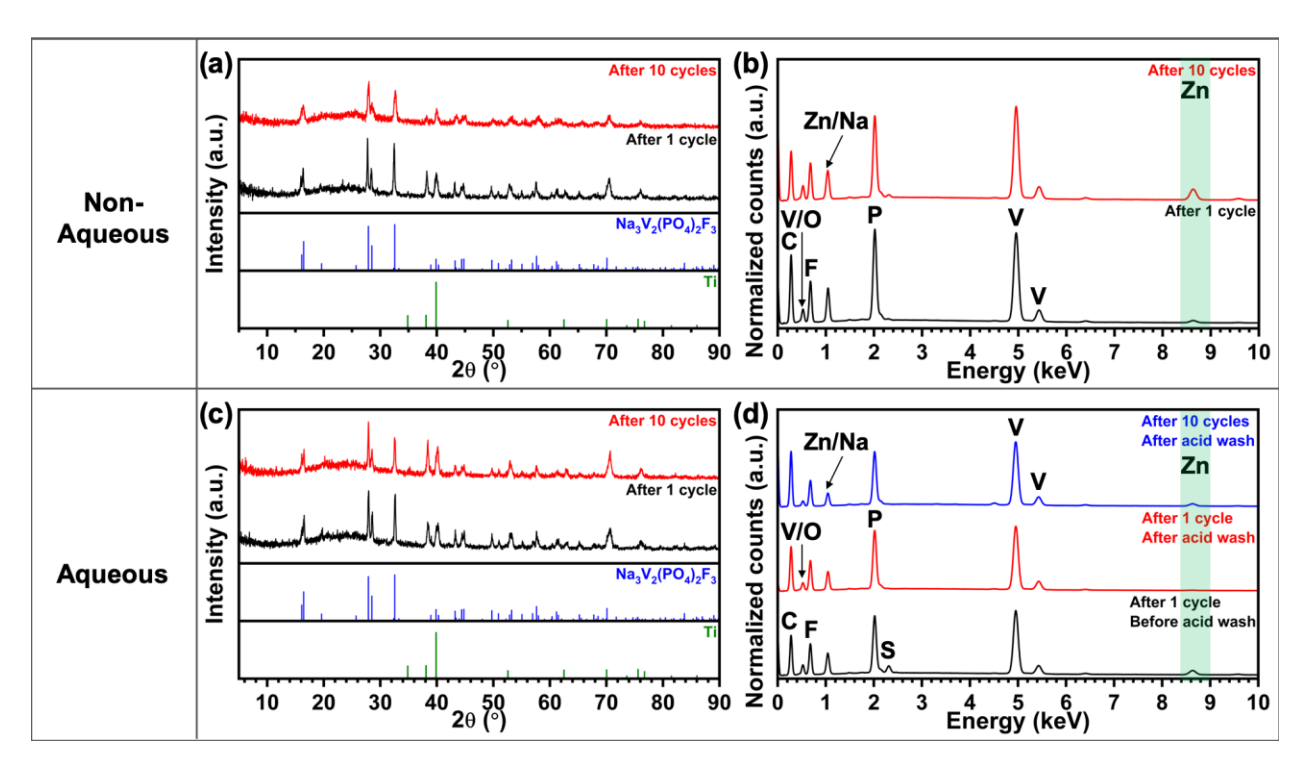


Figure 3. (a) XRD patterns and (b) EDX spectra of NVPF/C electrode after 1st and 10th cycles in non-aqueous Zn-ion cells. (c) XRD patterns and (d) EDX spectra of NVPF/C electrode after 1st and 10th cycles in aqueous Zn-ion cells.

The XRD patterns of the NVPF/C cathodes after the 1st and 10th cycles in the non-aqueous Zn-ion cells are displayed in Figure 3a. Since no reported structural data are available for Na₂Zn_xV₂(PO₄)₂F₃ (i.e., after Zn-insertion into Na₂V₂(PO₄)₂F₃), the reference peak markers of the NVPF phase are also presented for a comparison, as are those of Ti due to the use of Ti foil as the cathode current collector. After the 1st cycle (black), the acquired XRD pattern consists only of reflections that match well with the peak markers of the NVPF and Ti reference patterns presented below. This indicates that after the removal of one Na per formula unit of NVPF during the charge step, guest-ion insertion into the host transforms it into a phase similar to that of NVPF during the discharge step. In the corresponding elemental analysis via EDX scan in Figure 3b (black), Zn signal is present in the spectrum (green bar, Figure 3b) as anticipated along with those of other constituent elements of NVPF/C, confirming that Zn²⁺ is indeed inserted into the structure during the discharge step. The amount of Zn per formula unit of NVPF/C from the EDX spectrum is found to be 0.1. This explains the broad cathodic reduction current response in Figure 2d. Even at a slow scan rate of 50 µV s⁻¹, when Zn ions are the guest ions to NVPF/C host, their insertion and diffusion into the bulk would be kinetically limited due to the strong host-guest interaction.

From the same EDX spectrum, however, it is also evident that reinsertion of some of the extracted Na⁺ occurs during the discharge step. The amount of Na per formula unit of NVPF/C calculated from the acquired EDX spectrum is 2.5, which is 25% higher than the expected value of 2 after Na⁺ extraction during the charge step. This illustrates that co-insertion of Zn²⁺ and Na⁺ into NVPF/C host occurs in the non-aqueous system. This kind of co-insertion of alkali ions extracted from a host with multivalent ions during the discharge step has also been observed with Mg²⁺ insertion into Na_{0.69}Fe₂(CN)₆ and Zn²⁺ insertion into Na₃V₂(PO₄)₃.^{39,40} The Na⁺ reinsertion in NVPF/C host explains the relatively sharp anodic peaks and the plateau in the charge profiles

in Figure 2d,e. The more facile Na⁺ extraction occurs during the anodic scan, as evident by the decrease in the amount of Na per formula unit of the cathode from 2.5 to 1.8 (28% decrease), calculated from the EDX scan of the cathode after 2nd charge, while the amount of Zn per formula unit of the cathode remains similar at 0.15.

The fact that Zn ions are the guest ions also explains the poor reversibility of NVPF/C cathode in the non-aqueous system. Because the electrolyte originally was prepared to contain only Zn²⁺ as the cations, as cycling progresses, the extracted Na⁺ will diffuse away from the cathode and fewer and fewer Na ions would be reinserted into the structure with each cycle. As a result, the guest ions inserted and extracted for the faradaic reaction of NVPF/C will gradually shift from Na⁺/Zn²⁺ to pure Zn²⁺. This change would require more overpotential for the faradaic reactions to occur due to the sluggish diffusion of Zn²⁺ in the NVPF/C caused by the strong host-guest interaction. This is observed from the continuous broadening and shifting of the anodic peak in the CV to higher potentials with cycle number (Figure S3). It can thus be deduced that the rapid capacity fade during the galvanostatic cycling at 0.3 C in the non-aqueous system (Figure 2f) is because of the kinetic trapping of the inserted Zn ions in the host, which is due to the overpotential required to overcome the strong host-guest interaction. This claim is further supported by the fact that there is a significant increase in the intensity of the Zn signal in the EDX scan after 10 cycles (red, Figure 3b), and that the XRD patterns of NVPF/C after 1 and 10 charge/discharge cycles (red, Figure 3a) are similar despite the capacity fade. Moreover, the broadened diffraction peaks between 27 and 29 ° and at 32.5 ° after 10 cycles compared to those after 1 cycle aligns with the observed accumulation of Zn as it leads to a higher degree of lattice distortion due to the strong ionic interactions between Zn and O as discovered in our previous study.²²

In Figure 3c, the XRD patterns of NVPF/C cathodes after cycling in the aqueous Zn-ion cells are presented along with the reference peak markers for NVPF and Ti. For both the 1st (black) and 10th (red) cycles, the acquired XRD patterns match well with the peak markers of NVPF like those of NVPF/C cathodes after cycling in the non-aqueous Zn-ion cell. This indicates that even in the aqueous Zn-ion cell, NVPF/C undergoes a similar phase transformation during the discharge step, as expected. Corresponding EDX analyses on the electrodes after the 1st and 10th cycles in the aqueous Zn-ion cells, however, reveal a different story (Figure 3d).

The EDX spectrum of NVPF/C cathode after one cycle in the aqueous Zn-ion cell (black, Figure 3d) showed the presence of Zn in the electrode. But also, there was a noticeable S signal, illustrating that there is a sulfur-containing byproduct on the electrode, which only could have come from the anionic species of the zinc electrolyte, CF₃SO₃⁻. In order to remove this byproduct, the electrode was washed with HCl (pH 2). After washing with HCl, the S signal on the EDX spectrum (red, Figure 3d) disappeared demonstrating that the sulfur-containing byproduct was eliminated. Interestingly after the acid wash, the Zn signal also disappeared as evident on the EDX spectrum. It was determined previously that the 1st cycle discharge capacity of NVPF/C in the aqueous Zn-ion cell is 61 mA h g⁻¹, which is close to its theoretical capacity for one electron transfer. This means that the guest ions must have diffused into the bulk to compensate for the stored electrons. Since the bulk of the material remained intact after acid washing as evident by the strong signals of the constituent elements of NVPF/C, if the guest ions in the cathode were Zn²⁺, then Zn should have been detected. As no Zn signal is observable in the EDX spectrum after the acid wash, it can be inferred that in the aqueous Zn-ion cell, Zn²⁺ does not act as the charge balancing cation in the cathode. Instead, that Zn must be a part of the byproduct that was washed away with the acid. Also, the atomic ratio of Na per formula unit of the cathode is determined to

be 1.98 from the EDX scan of the cathode after the 1st cycle, which is close to the expected value of 2 after the removal of Na⁺ from the first charging step. From this, it can be inferred that Na⁺ is also not the charge balancing cation. Since no other free cations are present, it can be deduced that H⁺ ions act as the charge balancing cations rather than Zn²⁺. This not only explains the peak-like current response during the cathodic scan of the CV (Figure 2a), but also the excellent rate capabilities (16C) exhibited by the NVPF/C cathode in a recent report, 21 because of facile diffusion of H⁺ into the host structure. The Zn signal on the EDX spectrum of the acid washed electrode after 10 cycles (red, Figure 3d) indicates that some Zn²⁺ does get inserted into the host as cycling progresses. Having observed that Zn²⁺ insertion in NVPF/C is possible even at room temperature in the non-aqueous Zn-ion cell, it is sensible that over time some Zn²⁺ would have inserted along with H⁺ into the structure. However, as in the case of Zn-insertion in the non-aqueous Zn-ion cell, the Zn in the structure would remain kinetically trapped, contributing to the observed capacity fade during cycling of the aqueous Zn-ion cell. In this respect, for a better cycling performance of the aqueous Zn-ion cell, a higher cycling rate would be favored to minimize the possibility of Zn²⁺ insertion over H⁺.

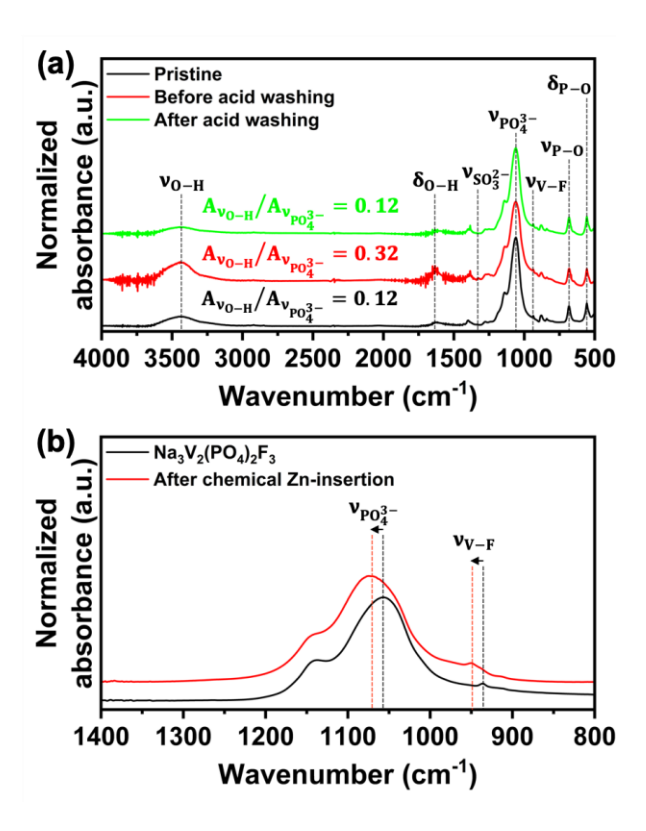


Figure 4. FT-IR spectra of (a) NVPF/C cathodes before and after one cycle in aqueous Zn-ion cells and (b) Na₃V₂(PO₄)₂F₃ powder before and after chemical Zn-insertion.

In addition, results from FT-IR analyses presented in Figure 4 provide further evidence for the conclusions deduced from the *ex-situ* structural and elemental analyses. Figure 4a shows the FT-IR spectra between 500 and 4,000 cm⁻¹ of NVPF/C cathode in its pristine state (black), after one cycle in aqueous Zn-ion cell before washing with acid (red), and after one cycle in aqueous Zn-ion cell after washing with acid (green). Absorbance bands characteristic of NVPF can be observed at low wavenumbers. Bending (δ_{P-O}) and stretching (ν_{P-O}) vibration bands of the P-O bond in NVPF arise, respectively, at 556 cm⁻¹ and 681 cm⁻¹. Also, a broad band due to asymmetric stretching vibration of the PO₄³⁻ tetrahedra (ν_{PO43-}) can be found at 1,063 cm⁻¹. A weak band at 936 cm⁻¹ signifies absorbance due to stretching vibration of the V-F bond (ν_{V-F}) in the structure.³⁷ Moreover, the signatures of O-H bond bending (δ_{O-H}) and stretching (ν_{O-H}) vibrations can be seen,

respectively, at 1,633 cm⁻¹ and 3,440 cm⁻¹. Figure 4b shows the absorbance spectra between 800 and 1,400 cm⁻¹ of NVPF powder in its pristine state (black) and after chemical Zn-insertion into the de-sodiated NVPF obtained by chemical oxidation (red). Chemical Zn-insertion was achieved *via* microwave-assisted iodide reduction method as demonstrated in our previous study.²² XRD and EDX analyses on the powder in Figure S4 clearly show that 0.35 Zn per formula unit is in the NVPF structure.

As evident in Figure 4b, v_{PO43-} band shifts from 1,063 cm⁻¹ to 1,074 cm⁻¹ and v_{V-F} band shifts from 936 cm⁻¹ to 950 cm⁻¹ after chemical Zn-insertion into the de-sodiated structure of NVPF. This is suspected to occur due to the insertion and coordination of much smaller but more charge dense Zn^{2+} cations that would affect the bonds in the host framework differently compared to the Na⁺ cations. Similar changes in the v_{PO43-} band wavenumber observed with Li₃V₂(PO₄)₃—another polyanionic host—with variations in the Li⁺ coordination in the structure supports this finding. Hence, if Zn ions are inserted into the structure of NVPF as guest ions during the electrochemical discharge step, similar shifts in the absorbance bands should be observed in the FT-IR spectrum. However, this shift in the absorbance bands is absent in the FT-IR spectra of electrodes after charge and discharge (one cycle) in aqueous Zn-ion cells (Figure 4a). This is another evidence to support that Zn²⁺ is not the guest ions for the faradaic reactions at NVPF/C cathode in the aqueous ZIBs.

Another feature of interest in Figure 4a is the significant difference in the absorbance of v_{O-H} band between the samples. The ratio of absorbance of the v_{O-H} band (Av_{O-H}) to that of the v_{PO43-} band (Av_{PO43-}) for the electrode before acid wash is 0.32, which is almost three times as high as that of the pristine electrode (0.12). The decrease in this ratio back to 0.12 after acid washing illustrates that the byproduct that forms on the electrode in the aqueous Zn-ion cell

contains an OH⁻ group. Noticeable spikes are present at 1,500 cm⁻¹, 1,650 cm⁻¹, and 3,750 cm⁻¹ in the spectrum for the electrode before acid wash. This is believed to be due to the absorption by minor amounts of water vapor in the sample chamber introduced during sample insertion. However, this does not affect the absorbance of the $\nu_{\text{O-H}}$ band. Also, the asymmetric stretching band of $SO_3{}^{2-}$ group in the CF₃SO₃⁻ (v_{SO32}-) at 1,326 cm⁻¹ can be observed after cycling in an aqueous Zn-ion cell (red, Figure 4a).⁴² Combined with the result of the elemental analysis (presence of significant Zn and S signal) of the electrode after one cycle before acid wash, it can be deduced that this byproduct takes some form of a zinc salt incorporating the OH⁻ group as well as the CF₃SO₃⁻ anionic group. This is in line with the findings in reports on oxide cathodes in aqueous ZIBs with both ZnSO₄ and Zn(CF₃SO₃)₂ electrolytes.^{7,29–31} Reports show that H⁺ insertion into the oxide hosts during discharge triggers concurrent byproduct formation. With ZnSO₄ electrolyte, the byproduct that forms on the electrode is hydrated zinc hydroxy sulfate salt (Zn₄(OH)₆(SO₄).xH₂O, x = 0, 0.5, 1, 3, 4, and 5), which is a layered double hydroxide (LDH) phase. With Zn(CF₃SO₃)₂ electrolyte, a similar LDH phase that also contains the CF₃SO₃⁻ anionic group is found to form, although further studies are required to determine its exact chemical formula. The observed presence of the zinc salt byproduct on NVPF/C cathode after discharge further supports that H⁺, rather than Zn²⁺, inserts into the host structure in the aqueous Zn-ion cell, as seen with other oxide hosts. Hence, the overall electrochemical equation for NVPF/C in the aqueous ZIB is proposed as follows:

$$Na_{2}V_{2}(PO_{4})_{2}F_{3} + \frac{x}{2}Zn + (x+n)H_{2}O + \frac{y}{2}Zn(CF_{3}SO_{3})_{2} \rightleftharpoons H_{x}Na_{2}V_{2}(PO_{4})_{2}F_{3} +$$

$$Zn_{\underline{(x+y)}}(CF_{3}SO_{3})_{y}(OH)_{x}.nH_{2}O \quad (0 \le x \le 1)$$

$$(1)$$

Moreover, preferential formation of Zn-only phases next to the cathode was discovered even in

aqueous Zn(NO₃)₂ electrolyte.⁴³ This suggests that the zinc salt byproduct formation may be a general issue that occurs in aqueous ZIB systems.

4. CONCLUSION

Here, a three-dimensional polyanionic NVPF/C with an open-framework structure, which has been claimed to be a host for reversible Zn²⁺ insertion is selected and investigated to clarify the apparent difference in its electrochemical behavior as a cathode in the non-aqueous and aqueous ZIB systems. Electrochemical cycling and ex-situ analyses of the cathode reveal a completely contrasting electrochemical behavior between the two systems, which stems from the difference in the guest ion for the faradaic reactions during cycling. In the non-aqueous ZIB system, the guest ions are determined to be Zn²⁺ with some Na⁺ that comes from NVPF/C host, but progressively shifts to be just Zn²⁺ with cycling. Even in the three-dimensional open-framework structure of NVPF/C, which is considered to be beneficial, Zn²⁺ diffusion in the host is determined to be sluggish due to the strong host-guest interaction. Hence, Zn²⁺ becomes kinetically trapped in the host during galvanostatic cycling at a rate of 0.3C, resulting in a rapid capacity fade. In the aqueous ZIB system, however, the guest ion for the faradaic reactions at the cathode is found to be H⁺ rather than Zn²⁺. This explains the observed stable galvanostatic cycling at a higher rate of 1C, and the reported excellent electrochemical performance of NVPF/C in aqueous ZIB.²¹ In addition, the formation of a zinc salt byproduct on the cathode with the Zn(CF₃SO₃)₂ electrolyte in the aqueous ZIB system is observed. As H⁺ is inserted into NVPF/C during discharge, the zinc salt byproduct containing Zn²⁺, CF₃SO₃⁻, and OH⁻ concurrently forms. A similar phenomenon is known to occur also with ZnSO₄ electrolyte, another commonly used electrolyte for aqueous ZIBs.

The formation of zinc salt byproduct on a cathode in an aqueous ZIB system could easily mislead researchers to think that Zn ions are the guest ions for faradaic reactions at a given cathode. In this specific case, acid washing was used to eliminate any contribution of the zinc salt byproduct for the *ex-situ* analyses because NVPF is a polyanionic host material that can withstand acid for some time due to its chemical stability. However, this may not be the case for various other cathode materials that have been investigated to date. Elucidating the charge-storage mechanism of each cathode material is essential for future development of ZIBs as well as other multivalent-ion batteries for higher energy density. Hence, careful analyses with suitable methods are warranted when exploring cathodes for aqueous "Zn-ion" batteries to unambiguously show that Zn ions are indeed the guest ions for the faradaic reactions at the cathode.

ASSOCIATED CONTENT

Supporting Information

The Supporting Information is available free of charge on the ACS Publications website at DOI:

A plot of change in mass against temperature obtained from TGA of NVPF/C; a plot of specific charge/discharge capacity versus cycle number for NVPF/C cathode cycled in an aqueous ZIB; CV of NVPF/C in a non-aqueous Zn-ion cell; XRD of NVPF and chemically oxidized and Zn-inserted NVPF powder, and EDX of the Zn-inserted powder; and a table of results of Rietveld refinement on the powder XRD of NVPF/C (PDF)

AUTHOR INFORMATION:

Corresponding Author

*E-mail: manth@austin.utexas.edu.

ORCID

Min Je Park: 0000-0003-1528-4758

Arumugam Manthiram: 0000-0003-0237-9563

Notes

The authors declare no competing financial interest.

ACKNOWLEDGMENTS

This work was supported by the Welch Foundation grant F-1254 and National Science Foundation,

Division of Materials Research, under award number 1709081.

REFERENCES

- (1) Liu, J.; Bao, Z.; Cui, Y.; Dufek, E. J.; Goodenough, J. B.; Khalifah, P.; Li, Q.; Liaw, B. Y.; Liu, P.; Manthiram, A.; Meng, Y. S.; Subramanian, V. R.; Toney, M. F.; Viswanathan, V. V.; Whittingham, M. S.; Xiao, J.; Xu, W.; Yang, J.; Yang, X.-Q.; Zhang, J.-G. Pathways for Practical High-Energy Long-Cycling Lithium Metal Batteries. *Nat. Energy* **2019**, *4*, 180–186.
- (2) Slater, M. D.; Kim, D.; Lee, E.; Johnson, C. S. Sodium-Ion Batteries. *Adv. Funct. Mater.* **2013**, *23*, 947–958.
- (3) Grey, C. P.; Tarascon, J. M. Sustainability and *in situ* Monitoring in Battery Development. *Nat. Mater.* **2017**, *16*, 45–56.
- (4) Canepa, P.; Sai Gautam, G.; Hannah, D. C.; Malik, R.; Liu, M.; Gallagher, K. G.; Persson, K. A.; Ceder, G. Odyssey of Multivalent Cathode Materials: Open Questions and Future Challenges. *Chem. Rev.* **2017**, *117*, 4287–4341.
- (5) Song, M.; Tan, H.; Chao, D.; Fan, H. J. Recent Advances in Zn-Ion Batteries. *Adv. Funct. Mater.* **2018**, *28*, 1802564.
- (6) Kaveevivitchai, W.; Manthiram, A. High-Capacity Zinc-Ion Storage in an Open-Tunnel Oxide for Aqueous and Nonaqueous Zn-Ion Batteries. *J. Mater. Chem. A* **2016**, *4*, 18737–18741.
- (7) Pan, H.; Shao, Y.; Yan, P.; Cheng, Y.; Han, K. S.; Nie, Z.; Wang, C.; Yang, J.; Li, X.; Bhattacharya, P.; Mueller, K. T.; Liu, J. Reversible Aqueous Zinc/Manganese Oxide Energy Storage from Conversion Reactions. *Nat. Energy* **2016**, *1*, 16039.
- (8) Xu, C.; Li, B.; Du, H.; Kang, F. Energetic Zinc Ion Chemistry: The Rechargeable Zinc Ion Battery. *Angew. Chem. Int. Ed.* **2012**, *51*, 933–935.
- (9) Alfaruqi, M. H.; Mathew, V.; Gim, J.; Kim, S.; Song, J.; Baboo, J. P.; Choi, S. H.; Kim, J. Electrochemically Induced Structural Transformation in a γ-MnO₂ Cathode of a High Capacity Zinc-Ion Battery System. *Chem. Mater.* **2015**, *27*, 3609–3620.
- (10) Lee, J.; Ju, J. B.; Cho, W. I.; Cho, B. W.; Oh, S. H. Todorokite-Type MnO₂ as a Zinc-Ion Intercalating Material. *Electrochim. Acta* **2013**, *112*, 138–143.
- (11) Wei, C.; Xu, C.; Li, B.; Du, H.; Kang, F. Preparation and Characterization of Manganese Dioxides with Nano-Sized Tunnel Structures for Zinc Ion Storage. *J. Phys. Chem. Solids* **2012**, *73*, 1487–1491.
- (12) Zhang, N.; Cheng, F.; Liu, Y.; Zhao, Q.; Lei, K.; Chen, C.; Liu, X.; Chen, J. Cation-Deficient Spinel ZnMn₂O₄ Cathode in Zn(CF₃SO₃)₂ Electrolyte for Rechargeable Aqueous Zn-Ion Battery. *J. Am. Chem. Soc.* **2016**, *138*, 12894–12901.
- (13) Sun, W.; Wang, F.; Hou, S.; Yang, C.; Fan, X.; Ma, Z.; Gao, T.; Han, F.; Hu, R.; Zhu, M.; Wang, C. Zn/MnO₂ Battery Chemistry With H⁺ and Zn²⁺ Coinsertion. *J. Am. Chem. Soc.* **2017**, *139*, 9775–9778.
- (14) Kundu, D.; Adams, B. D.; Duffort, V.; Vajargah, S. H.; Nazar, L. F. A High-Capacity and Long-Life Aqueous Rechargeable Zinc Battery Using a Metal Oxide Intercalation Cathode. *Nat. Energy* **2016**, *1*, 16119.
- (15) Alfaruqi, M. H.; Mathew, V.; Song, J.; Kim, S.; Islam, S.; Pham, D. T.; Jo, J.; Kim, S.; Baboo, J. P.; Xiu, Z.; Lee, K.-S.; Sun, Y.-K.; Kim, J. Electrochemical Zinc Intercalation in Lithium Vanadium Oxide: A High-Capacity Zinc-Ion Battery Cathode. *Chem. Mater.* **2017**, *29*, 1684–1694.

- (16) Wan, F.; Zhang, L.; Dai, X.; Wang, X.; Niu, Z.; Chen, J. Aqueous Rechargeable Zinc/Sodium Vanadate Batteries with Enhanced Performance from Simultaneous Insertion of Dual Carriers. *Nat. Commun.* **2018**, *9*, 1656.
- (17) Kundu, D.; Vajargah, S. H.; Wan, L.; Adams, B.; Prendergast, D.; Nazar, L. F. Aqueous vs. Nonaqueous Zn-Ion Batteries: Consequences of the Desolvation Penalty at the Interface. *Energy Environ. Sci.* **2018**, *11*, 881–892.
- (18) Zhang, L.; Chen, L.; Zhou, X.; Liu, Z. Towards High-Voltage Aqueous Metal-Ion Batteries Beyond 1.5 V: The Zinc/Zinc Hexacyanoferrate System. *Adv. Energy Mater.* **2015**, *5*, 1400930.
- (19) Jia, Z.; Wang, B.; Wang, Y. Copper Hexacyanoferrate with a Well-Defined Open Framework as a Positive Electrode for Aqueous Zinc Ion Batteries. *Mater. Chem. Phys.* **2015**, *149–150*, 601–606.
- (20) Li, G.; Yang, Z.; Jiang, Y.; Jin, C.; Huang, W.; Ding, X.; Huang, Y. Towards Polyvalent Ion Batteries: A Zinc-Ion Battery Based on NASICON Structured Na₃V₂(PO₄)₃. *Nano Energy* **2016**, *25*, 211–217.
- (21) Li, W.; Wang, K.; Cheng, S.; Jiang, K. A Long-Life Aqueous Zn-Ion Battery Based on Na₃V₂(PO₄)₂F₃ Cathode. *Energy Storage Mater.* **2018**, *15*, 14–21.
- (22) Park, M. J.; Yaghoobnejad Asl, H.; Therese, S.; Manthiram, A. Structural Impact of Zn-Insertion into Monoclinic V₂(PO₄)₃: Implications for Zn-Ion Batteries. *J. Mater. Chem. A* **2019**, 7, 7159–7167.
- (23) Knight, J. C.; Therese, S.; Manthiram, A. On the Utility of Spinel Oxide Hosts for Magnesium-Ion Batteries. *ACS Appl. Mater. Interfaces* **2015**, 7, 22953–22961.
- (24) Knight, J. C.; Therese, S.; Manthiram, A. Chemical Extraction of Zn from ZnMn₂O₄-Based Spinels. *J. Mater. Chem. A* **2015**, *3*, 21077–21082.
- (25) Okamoto, S.; Ichitsubo, T.; Kawaguchi, T.; Kumagai, Y.; Oba, F.; Yagi, S.; Shimokawa, K.; Goto, N.; Doi, T.; Matsubara, E. Intercalation and Push-Out Process with Spinel-to-Rocksalt Transition on Mg Insertion into Spinel Oxides in Magnesium Batteries. *Adv. Sci.* **2015**, *2*, 1500072.
- (26) Shimokawa, K.; Atsumi, T.; Harada, M.; E. Ward, R.; Nakayama, M.; Kumagai, Y.; Oba, F.; L. Okamoto, N.; Kanamura, K.; Ichitsubo, T. Zinc-Based Spinel Cathode Materials for Magnesium Rechargeable Batteries: Toward the Reversible Spinel–Rocksalt Transition. *J. Mater. Chem. A* **2019**, *7*, 12225–12235.
- (27) Fang, G.; Zhou, J.; Pan, A.; Liang, S. Recent Advances in Aqueous Zinc-Ion Batteries. *ACS Energy Lett.* **2018**, *3*, 2480–2501.
- (28) Wang, C.; Wang, M.; He, Z.; Liu, L.; Huang, Y. Rechargeable Aqueous Zinc–Manganese Dioxide/Graphene Batteries with High Rate Capability and Large Capacity. *ACS Appl. Energy Mater.* **2020**, *3*, 1742–1748.
- (29) Wang, L.; Huang, K.-W.; Chen, J.; Zheng, J. Ultralong Cycle Stability of Aqueous Zinc-Ion Batteries with Zinc Vanadium Oxide Cathodes. *Sci. Adv.* **2019**, *5*, eaax4279.
- (30) Lee, B.; Seo, H. R.; Lee, H. R.; Yoon, C. S.; Kim, J. H.; Chung, K. Y.; Cho, B. W.; Oh, S. H. Critical Role of pH Evolution of Electrolyte in the Reaction Mechanism for Rechargeable Zinc Batteries. *ChemSusChem* **2016**, *9*, 2948–2956.
- (31) Oberholzer, P.; Tervoort, E.; Bouzid, A.; Pasquarello, A.; Kundu, D. Oxide versus Nonoxide Cathode Materials for Aqueous Zn Batteries: An Insight into the Charge Storage Mechanism and Consequences Thereof. *ACS Appl. Mater. Interfaces* **2019**, *11*, 674–682.

- (32) Zhang, L.; Miao, L.; Zhang, B.; Wang, J.; Liu, J.; Tan, Q.; Wan, H.; Jiang, J. A Durable VO₂(M)/Zn Battery with Ultrahigh Rate Capability Enabled by Pseudocapacitive Proton Insertion. *J. Mater. Chem. A* **2020**, *8*, 1731–1740.
- (33) Li, L.; Hoang, T. K. A.; Zhi, J.; Han, M.; Li, S.; Chen, P. Functioning Mechanism of the Secondary Aqueous Zn-β-MnO₂ Battery. *ACS Appl. Mater. Interfaces* **2020**, *12*, 12834–12846.
- (34) Toby, B. H.; Von Dreele, R. B. GSAS-II: The Genesis of a Modern Open-Source All Purpose Crystallography Software Package. *J. Appl. Cryst.* **2013**, *46*, 544–549.
- (35) Gover, R. K. B.; Bryan, A.; Burns, P.; Barker, J. The Electrochemical Insertion Properties of Sodium Vanadium Fluorophosphate, Na₃V₂(PO₄)₂F₃. *Solid State Ion.* **2006**, *177*, 1495–1500.
- (36) Bianchini, M.; Brisset, N.; Fauth, F.; Weill, F.; Elkaim, E.; Suard, E.; Masquelier, C.; Croguennec, L. Na₃V₂(PO₄)₂F₃ Revisited: A High-Resolution Diffraction Study. *Chem. Mater.* **2014**, *26*, 4238–4247.
- (37) Li, L.; Xu, Y.; Sun, X.; Chang, R.; Zhang, Y.; Zhang, X.; Li, J. Fluorophosphates from Solid-State Synthesis and Electrochemical Ion Exchange: NaVPO₄F or Na₃V₂(PO₄)₂F₃? *Adv. Energy Mater.* **2018**, *8*, 1801064.
- (38) Bianchini, M.; Fauth, F.; Brisset, N.; Weill, F.; Suard, E.; Masquelier, C.; Croguennec, L. Comprehensive Investigation of the Na₃V₂(PO₄)₂F₃–NaV₂(PO₄)₂F₃ System by Operando High Resolution Synchrotron X-Ray Diffraction. *Chem. Mater.* **2015**, *27*, 3009–3020.
- (39) Kim, D.-M.; Kim, Y.; Arumugam, D.; Woo, S. W.; Jo, Y. N.; Park, M.-S.; Kim, Y.-J.; Choi, N.-S.; Lee, K. T. Co-Intercalation of Mg²⁺ and Na⁺ in Na_{0.69}Fe₂(CN)₆ as a High-Voltage Cathode for Magnesium Batteries. *ACS Appl. Mater. Interfaces* **2016**, *8*, 8554–8560.
- (40) Hu, P.; Zhu, T.; Wang, X.; Zhou, X.; Wei, X.; Yao, X.; Luo, W.; Shi, C.; Owusu, K. A.; Zhou, L.; Mai, L. Aqueous Zn//Zn(CF₃SO₃)₂//Na₃V₂(PO₄)₃ Batteries with Simultaneous Zn²⁺/Na⁺ Intercalation/de-Intercalation. *Nano Energy* **2019**, *58*, 492–498.
- (41) Burba, C. M.; Frech, R. Vibrational Spectroscopic Studies of Monoclinic and Rhombohedral Li₃V₂(PO₄)₃. *Solid State Ion.* **2007**, *177*, 3445–3454.
- (42) Wendsjö, Å.; Lindgren, J.; Paluszkiewicz, C. Structure, Dynamics and Morphology in the System M(CF₃SO₃)₂ PEO_n for M = Zn and Pb. *Electrochim. Acta* **1992**, *37*, 1689–1693.
- (43) Nolis, G. M.; Adil, A.; Yoo, H. D.; Hu, L.; Bayliss, R. D.; Lapidus, S. H.; Berkland, L.; Phillips, P. J.; Freeland, J. W.; Kim, C.; Klie, R. F.; Cabana, J. Electrochemical Reduction of a Spinel-Type Manganese Oxide Cathode in Aqueous Electrolytes with Ca²⁺ or Zn²⁺. *J. Phys. Chem. C* **2018**, *122*, 4182–4188.

TOC Figure

